STRUCTURE OF THE CHANNELS IN THE OUTER MITOCHONDRIAL MEMBRANE

Electron Microscopic Studies of the Periodic Arrays Induced by Phospholipase A_2 Treatment of the Neurospora Membrane

C. A. MANNELLA, A. RIBEIRO, AND J. FRANK
Wadsworth Center for Laboratories and Research, New York State Department of Health, Albany, New York 12201

ABSTRACT The channel proteins in outer membranes of *Neurospora crassa* mitochondria spontaneously organize into periodic arrays when the membranes are dialyzed in the presence of soluble phospholipase A_2. Electron microscopic images have been recorded at different electron doses from channel arrays in a variety of negative stains, as well as in vitreous ice. Fourier or correlation averages are formed from image fields containing a few hundred unit cells. These averages can be subsequently classified by correspondence analysis and summed to form representative averages over thousands of unit cells. In averages of negatively stained arrays, the stain-filled channel openings are bounded by smaller stain-excluding maxima. The projections of the channel openings are smaller and the subsidiary maxima are more pronounced for channel arrays contrasted with dilute (0.1%) uranyl acetate or aurothioglucose than for arrays embedded in 1% uranyl acetate. Projection images of unstained, ice-embedded membranes provide direct information about distribution of protein and lipid in the VDAC arrays. First experiments have yielded density maps with an apparent Fourier resolution of ~1/(2 nm).

INTRODUCTION

Periodic Arrays of Mitochondrial Outer Membrane Channels

The molecular basis for the extreme permeability of the mitochondrial outer membrane appears to be a class of 30,000 d integral polypeptides (1–3). These proteins have been named VDAC (for Voltage-Dependent, Anion-selective Channel) based on their functional characteristics when incorporated in phospholipid bilayers (4, 2). The mitochondrial outer membrane channels have also been called "mitochondrial porin," by analogy with the wide variety of passive diffusion channels that occur in outer envelopes of gram negative bacteria (3, 5).

The channel proteins in outer membranes of mitochondria of the fungus *Neurospora crassa* occur in planar crystalline arrays (6, 7). This characteristic of fungal VDAC has made possible the application of Fourier averaging techniques in electron microscopic studies of its structure (6–9). In Fourier-filtered, negative-stain images of the most commonly observed crystalline form of VDAC (a parallelogram array), the repeating motif is a group of six dense stain centers arranged on a hexagon with p2 symmetry (Fig. 1). Limited-resolution, three-dimensional analysis of a negatively stained VDAC array indicates that the stain accumulations are situated in an otherwise stain-free, horizontal zone spanning the central 4–5 nm of the reconstructed volume, consistent with stain-filled channels traversing a phospholipid bilayer (10). Unlike the case of *Escherichia coli* porin (11), there is no indication of lateral fusion of the stain-filled channels in the membrane interior. Also, there is no significant projecting mass in either the three-dimensional reconstruction or in edge-on views of folded VDAC arrays, consistent with the known resistance of the channel protein to proteases (1, 12).

Size of the VDAC Channel

There is considerable interest in correlating the physical dimensions of the aqueous, transmembrane compartments of biological channels with their permeability characteristics. Initially, one might expect negative stain electron microscopy to provide a direct indication of the interior shape of a channel like VDAC. Commonly used negative stains are heavy-metal salts that form a (more or less) amorphous, electron-dense cast around macromolecules. Because these salts are very water-soluble, they should fill the hydrophilic interior of an ion channel. If the channel is normal to the membrane plane, the diameter of the axial projection of the stain "cylinder" in the channel provides an upper limit to the channel bore. Subsequent three-dimensional analysis of the intrachannel stain distribution could detect variations in channel size along the transverse

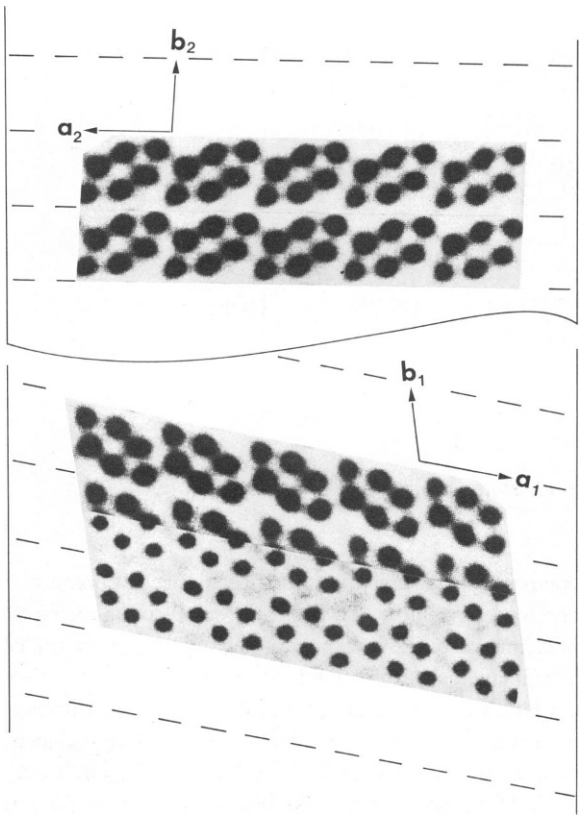

FIGURE 1 Geometry of parallelogram VDAC arrays. *Bottom*: Fourier filtered composite image of a normally observed parallelogram array (lattice angle = 108°) viewed from inside a cylindrical tube, indicating alignment of lattice vectors ($\mathbf{a}_1$, $\mathbf{b}_1$) relative to the sides of the tube (represented by straight vertical lines at horizontal distances not to scale with array images). Note the stain accumulations at the channel openings, larger with phosphotungstate (upper half of image) than with uranyl acetate (lower half of image). *Top*: Image of a VDAC array viewed from the outside of a tube, with the parallel rows of channel clusters running in the opposite direction relative to the inside view. In this array, the rows have slid relative to each other (lattice angle = 92°), resulting in shrinkage of the channel-free areas, a change associated with higher level phospholipase treatment. Note: in reality, lattice angles of top and bottom layers of a collapsed tube normally fall within 1° of each other.

direction. However, comparison of projection images of VDAC arrays embedded in different negative stains has indicated that the actual situation is not so simple (9). The diameters of the planar projections of the stain accumulations at the channel openings in crystalline VDAC vary with the negative stain used: ~2.5 nm with low-ionic-strength negative stains, such as uranyl acetate, vs. 3 nm with anionic stains with large dissociation constants, like phosphotungstate. Based on surface-charge modification experiments, excess accumulation of ionic stains at the channels has been attributed to binding at fixed charges on the channel protein (9). (Acidic and basic amino acids constitute about one-quarter of the residues of *N. crassa* VDAC, reference 12.) In the present report, the effect of the nature of the negative stain medium on the size and shape of the channel projections in computer-averaged VDAC images will be examined further. In addition the effects of radiation damage on projection images of the negatively stained channel arrays will be examined.

Imaging of Unstained VDAC Arrays

One of the most important questions currently being addressed in studies of biological membrane proteins is that of the secondary structure of the polypeptides in the phospholipid bilayer. The relative absence of projecting mass in the VDAC arrays means that it may be possible to get a "cleaner" view of the polypeptide forming the aqueous channel than is available with other model systems, such as gap junction connexons and acetylcholine receptors (13–16). Of course, direct visualization of the polypeptide in a membrane interior requires imaging unstained membrane arrays. Whether sufficient resolution can be obtained in two-dimensional and three-dimensional reconstructions of electron images of unstained VDAC arrays to distinguish the secondary structure of the channel-forming polypeptides is presently uncertain. A moderate-resolution (~1/[2 nm]) average of ice-embedded VDAC, formed by correlation averaging procedures from a few crystalline fields, is presented in the final section of this paper.

Phospholipase-Induced Crystallization of VDAC

The minimal-dose imaging experiments described below were made feasible in large part by the recent discovery that periodic arrays of VDAC can be reproducibly induced in fungal outer mitochondrial membranes by treatment of the membranes with soluble phospholipase A_2 (17). Yields of crystalline membranes in untreated *N. crassa* mitochondrial outer membrane fractions are variable, usually representing <10% of the total membrane population. Such preparations are unsuited for electron microscopy under low contrast conditions, especially when images are to be recorded "blind" to minimize specimen irradiation. However, treatment of the same mitochondrial outer membrane preparations with low levels of bee-venom phospholipase A_2 results in quantitative conversion of nonordered to ordered membranes. This change in ultrastructure is accompanied by decreased diameter and increased buoyant density of the outer mitochondrial membranes, presumably because of removal of the products of phospholipid hydrolysis from the membranes (17, 18).

MATERIALS AND METHODS

Phospholipase A_2 Treatment of Isolated Mitochondrial Outer Membranes

Outer membrane fractions were isolated from mitochondria of the fungus *N. crassa* (FGSC 326) by hypoosmotic lysis and sucrose step-gradient centrifugation using procedures described elsewhere (6, 18). These membranes are composed of 40% protein and 60% lipid by mass (19). The main lipid components are phospholipids and ergosterol (molar ratio 3:1);

the zwitterions phosphatidylcholine and phosphatidylethanolamine comprise two-thirds of the phospholipids, the remainder being mostly acidic moieties (phosphatidylserine, phosphatidylinositol, phosphatidic acid) (19). The principal protein component of the isolated mitochondrial outer membranes is the 31,000 d VDAC polypeptide (6, 12).

Freshly isolated mitochondrial outer membrane fractions are diluted to 1–10 μg protein/ml low-salt buffer (1 or 10 mM Tris-HCl, pH 7.5; 0.25 mM EDTA), and divided into three or four fractions, to which are added serial aliquots of bee-venom phospholipase A_2 (Sigma Chemical Company, St. Louis, MO); final concentrations of enzyme are in the range 0.2–2 units/ml. These membrane fractions are then dialyzed against a large volume of low-salt buffer in the cold for ~18 h. Following dialysis, the membranes are pelleted (100,000 × *g*, 90 min) and resuspended in a small volume of low-salt buffer to a final protein concentration of ~0.2 mg/ml. These suspensions are used directly for making electron microscopic specimens.

Conventional Negative-Stain Electron Microscopy

Negative stains used were aqueous solutions of uranyl acetate (1%, unadjusted pH 4.2), uranyl sulfate (1%, adjusted to pH 4.3 with NH_4OH), uranyl formate (saturated solution, ~0.5%, adjusted to pH 4.5 with NH_4OH) and uranyl oxalate (0.25%, adjusted to pH 6.8 with NH_40H). Five μl of membrane suspension and 5 μl stain were deposited and mixed on a freshly glow-discharged, carbon/formvar-coated copper grid. After 1–2 min, excess liquid was blotted off the grid surface, which was subsequently rinsed twice with stain, blotted, and air-dried. Specimens were examined in the electron microscope (100 kV, Philips EM 301 or 420-T, Philips Electronic Instruments, West Nyack, NY) within a few hours of preparation. Images were recorded on Kodak S0163 film (Eastman Kodak, Rochester, NY) at instrument magnifications (nominal) 49–57,000 ×.

Evaluation of Membrane Preparations by Optical Diffraction

Mitochondrial outer membrane fractions are routinely screened for content of VDAC arrays by optical diffraction from electron microscopic images, using coherent radiation from a He-Ne laser (Jodon Engineering Associates, Ann Arbor, MI). A typical, freshly isolated, negatively stained outer mitochondrial membrane is shown in Fig. 2 *A*: a flattened, roughly spherical vesicle with irregular edges, falling in a diameter range 0.2–1.5 μm. Membranes such as these generally show no evidence of ordered substructure (i.e., no regular, discrete reflections in optical diffraction patterns). Membranes like that shown in Fig. 2 *B* are common in fractions subjected to low-level phospholipase A_2 treatment. It has a less irregular outline than that of Fig. 2 *A* and shows indications of polycrystalline substructure, consistent with the diffuse reflections observed in its optical diffraction pattern. With increased phospholipase treatment, membranes composed entirely (or nearly so) of VDAC arrays, like those of Figs. 2 *C* and *D*, dominate the fractions. The first is a flattened tube whose optical diffraction pattern contains reflections that index on two parallelogram lattices related by mirroring and rotation (average lattice parameters: a = 12.6 nm, b = 11.1 nm, θ = 109°). The second membrane is a folded sheet composed of a rectangular array with a smaller unit cell (a = 8.7 nm, b = 5.1 nm). In general, rectangular VDAC arrays are more prevalent in membrane fractions treated with higher levels of phospholipase A_2, indicating that the rectangular array is derived from the parallelogram array with increased removal of phospholipids from the membranes.

The geometry of the parallelogram VDAC array is indicated in Fig. 1: it is a closed tube formed by rows of channel clusters (i.e., strips of unit cells parallel to the *a* lattice direction) wrapped around the long axis of the tube. The pitch of the rows and width of the tubes vary from membrane to membrane. It appears that, on average, each tubular membrane is a continuous wrapping of a set of ~10 parallel rows of channel clusters.

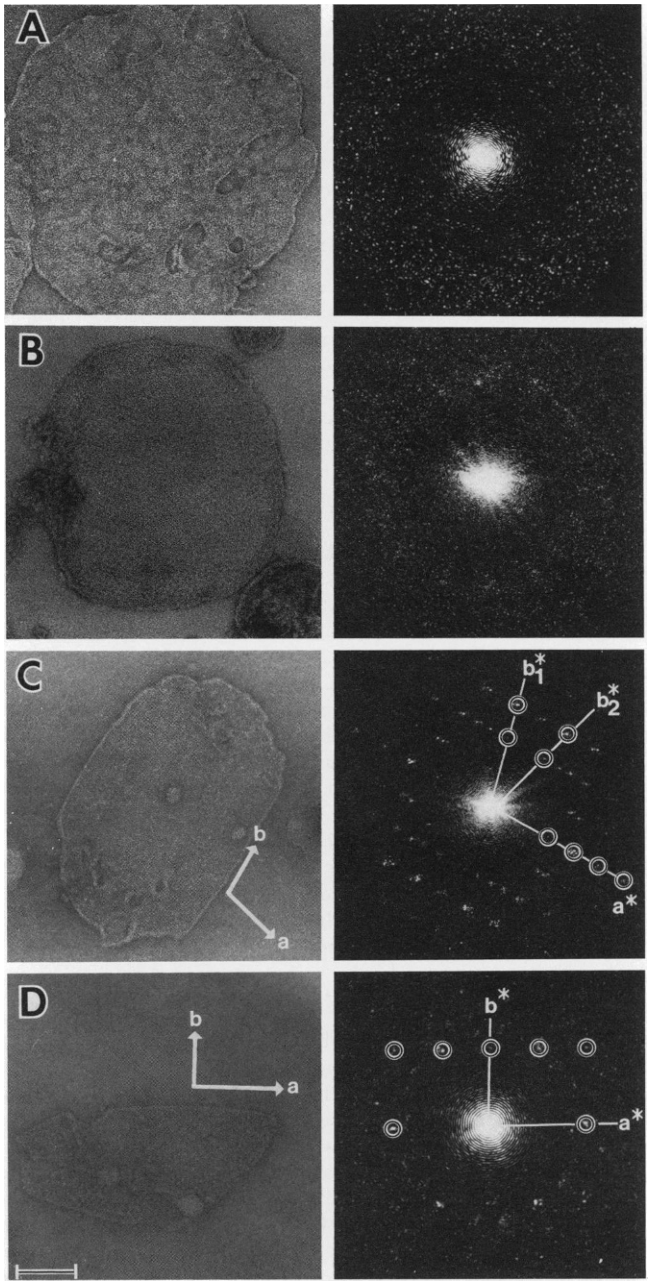

FIGURE 2 Stages of crystallization of VDAC in *N. crassa* mitochondrial outer membranes. *Left*: Electron microscopic images of membranes embedded in 1% uranyl acetate. *Right*: Optical diffraction patterns recorded from original electron image negatives. (*A*) Amorphous outer mitochondrial membrane. (*B*) Polycrystalline membrane. (*C*) Collapsed outer membrane tube composed of a parallelogram array. The principal axes of the two superimposed reciprocal lattices are indicated on the diffraction pattern. (The two **a*** directions coincide in this example, which is not normally the case.) The directions of the real-space lattice vectors corresponding to reciprocal lattice 1 are indicated in the micrograph. (*D*) Folded outer membrane sheet composed of a rectangular array. The two lattices very nearly coincide in the region (on the right side of the membrane) from which the diffraction pattern was recorded. The reciprocal and real space lattice directions are indicated as in (*C*). (Figure is reproduced with permission from reference 18.)

With increased phospholipase treatment, parallelogram arrays are observed with lattice angles <109° (see Figs. 1 and 5); the new geometry results from sliding of the rows such that the size of the channel-free areas (presumably phospholipid) is minimized (8). The compressed parallelogram arrays probably represent intermediate states in the transition from the normal parallelogram array to the rectangular array (8).

The present image processing studies have been restricted to parallelogram VDAC arrays. Thus, only membrane fractions containing predominantly tubular membranes were used for electron microscopic imaging.

Minimal-Irradiation Electron Microscopy

To decrease the total accumulated electron dose on the specimen during image recording, several changes were made in routine electron imaging procedures. A beam deflection accessory (Philips Model 6587, low-dose unit) was used in the EM 420 microscope, which allows focussing and astigmatism corrections to be made on fields adjacent to those being recorded. Because the membrane preparations used contained high percentages (generally ≥40%) of tubular VDAC arrays, fields could be recorded "blind," i.e., with no preirradiation. Additionally, the speed of the recording emulsion was pushed by a factor of 2.8 (by altering the developing conditions) allowing image recording at a total dose of 1–2 × 10^3 electrons/nm^2 (e/nm^2) (vs. accumulated doses >10^4 e/nm^2 in conventional electron image recording). In general, low-dose images are recorded under conditions otherwise similar to those normally used, i.e., exposures of ≤1 s with objective aperture of 50 μm and objective lens defocus of −150 to −300 nm.

Several different kinds of VDAC specimens have been imaged under low-irradiation conditions, including arrays air-dried in normal and dilute negative stain (1% and 0.1% uranyl acetate) and in thin layers of a heavy-metal-labeled sugar (1% aurothioglucose). Additionally, images have been obtained with unstained VDAC arrays embedded in vitreous ice. The latter specimens were frozen in liquid nitrogen and examined at −160°C in the EM 420 with the Philips Model 6599 cryo-holder.

Specimens for low-dose imaging experiments are deposited on grids bearing thin (5–10 nm thick) carbon films suspended across fenestrated carbon/formvar support films. Only images of arrays occuring over the holes in the thick support net are processed further.

Image Processing

Micrographs of parallelogram VDAC arrays were digitized with a flatbed scanning microdensitometer (PDS 1010A, Perkin Elmer, Garden Grove, CA). Scanning grids were used corresponding to sampling distances of 0.51 nm, except with conventional negative-stain images, for which a 0.88 nm grid was normally used.

Processing of digitized images of VDAC arrays was done using the SPIDER system (20), implemented on a VAX 11/780 computer (Digital Equipment Corp., Maynard, MA). Independent Fourier-averages of each layer in the superimposed arrays were calculated by a quasi-optical filtration procedure described in detail elsewhere (9). The procedure basically involves filtering the image transform with a mask defined by the reciprocal lattice corresponding to one VDAC array layer. The resolution limit in the filtered images (formed by inverse transformation of the masked transform) is effectively the reciprocal-space distance of the highest-order reflections in the original image transform.

For detailed comparisons of different images, small fields corresponding to one unit cell, bordered on each side by about one-half unit cell, were windowed from the center of Fourier-filtered fields. These images were then aligned rotationally and translationally by autocorrelation and cross-correlation analyses (21), after bilinear interpolation (to increase the accuracy of alignments) and magnification correction (based on reciprocal lattice parameters, see reference 9).

Correspondence analysis of Fourier-filtered images of unit cells of VDAC arrays corresponding to different negative stains was performed using algorithms previously applied to studies of images of single biomolecules (22).

The technique of correlation averaging has been developed to overcome limitations in Fourier averaging procedures imposed by lattice disorder (23, 24). Successful application of correlation averaging to images of overlapped, planar crystalline structure has recently been demonstrated (25). Conditions for obtaining independent averages of the two (or more) layers in such a structure are the same as those required for independent Fourier reconstruction, i.e., no superposition of reflections from the different overlapped arrays is allowed. The procedure used in the present study involves preliminary Fourier filtration of the field to be averaged, sampled at 0.51 nm and containing 100–300 unit cells. An area of 44 × 44 pixels centered on one cluster of six channels from one VDAC layer is windowed from the middle of the filtered field, padded into a 512 × 512 matrix, and cross-correlated with a 512 × 512 field in the unfiltered image. The resulting cross-correlation function contains peaks at locations in the large field where there is a strong match with the reference image. A peak-search program is used to define the precise coordinates of the cross-correlation peaks, which can subsequently be mapped into a 512 × 512 matrix for visual inspection. Such maps are useful for estimating the degree of lattice disorder in the arrays. Also, these maps indicate whether there are peaks in the cross-correlation function corresponding to the opposite array. When such "leakage" occurs (which is seldom), the correlation coefficients corresponding to the unwanted layer are generally small. The peak-search program contains an option to reject peaks that fall closer than a specified distance to peaks already identified. By making this distance slightly smaller than the smallest unit cell vector, peaks corresponding to the wrong VDAC layer can virtually be eliminated. Average images are subsequently formed by addition of small areas windowed from the raw field at the exact coordinates specified by the peak-search program.

RESULTS AND DISCUSSION

An Average, Conventional-Dose Image of Negatively Stained VDAC

To provide a basis for comparison between high- and low-dose electron images of VDAC arrays, an average high-dose image was calculated from Fourier-filtered projections of negatively stained arrays. In forming this average, images of the VDAC array embedded in several different uranyl salts were Fourier-averaged and classified by correspondence analysis.

A general problem encountered in interpreting negative stain images is the variability observed from one image to the next. Conventional statistical criteria can be used to determine the relatedness of images, such as calculations of R-factors for images of crystalline specimens and of total image variance in single-particle studies. However, while these statistical tests are useful for quantifying inter-image variability, they do not generally provide information about its nature.

Recently, correspondence analysis, a form of multivariate statistical analysis, has been used to determine the systematic differences in sets of negative-stain projection images (22). Briefly, an image consisting of p image elements can be represented as a p-dimensional vector whose component in each ith dimension has a length proportional to the optical density of the ith image element. A set of n aligned images forms a "cloud" of points defined in p-space by these image vectors. Correspondence analysis determines the orthogonal directions in p-space along which variance in the image cloud is greatest. When the

image cloud is projected into two-dimensional subspaces defined by these directions (called "factor axes"), images that are closely related will fall near each other. In addition, "importance images" can be calculated, which indicate the relative contribution of each image element to defining a particular factor axis. In effect, importance images of the factorial directions with highest variance reveal underlying patterns of differences in the image set.

For periodic specimens, correspondence analysis can be conveniently applied to diffraction patterns instead of images, greatly simplifying the alignment procedure. Such an analysis was done recently with condensed Fourier power spectra calculated from electron images of negatively stained VDAC arrays (9). Clustering of the diffraction patterns in the latter study indicated the existence of distinct stain distribution patterns associated with different types of negative stains. However, except in the simplest cases, importance patterns could not easily be interpreted directly in terms of differences in the associated images. Therefore, in the present study, we have applied correspondence analysis directly to Fourier-filtered unit-cell images of parallelogram VDAC arrays with the same lattice geometry (i.e., lattice angles = 108.5° ± 1.5°). For this analysis we have considered only images of VDAC arrays embedded in uranyl salts, because previous results indicate decreased high-resolution detail in projection images of arrays embedded in other negative stains (see Introduction).

The data set analyzed consisted of 32 aligned, Fourier-averaged VDAC images, each circularly masked (radius = 48 pixels) to include one group of six channels and eight nearest neighbors. The 32 images represented eight each of the following negative stains: uranyl acetate, uranyl oxalate, uranyl formate, and uranyl sulfate. Fig. 3 is a map of the projection of the image cloud onto the plane defined by the first two factor axes found by correspondence analysis. Superimposed on the map are representative members of the data set and the importance images associated with each direction along the factor axes. Factor axis 1 (vertical direction) accounts for 50% of the total interimage variance, compared with 10.5% for factor axis 2 (horizontal direction). The variance associated with lower factor axes decreases from 7% (factor axis 3) to <1% (factor axes 17–32). The large variance in the first few factorial directions suggests the presence of systematic (nonrandom) differences between the images in the data set. This conclusion is supported by the importance images associated with each direction along the two factor axes. Factor axis 1, which is clearly the statistically more significant, is associated with the relative density of stain within the channels vs. outside. The amount of stain outside the channel openings increases from top to bottom in the map. Factor axis 2 has to do with the relative amount of stain between adjacent channel openings within each group, which increases from left to right, giving rise to the appearance of stain cross-bridging, like that observed

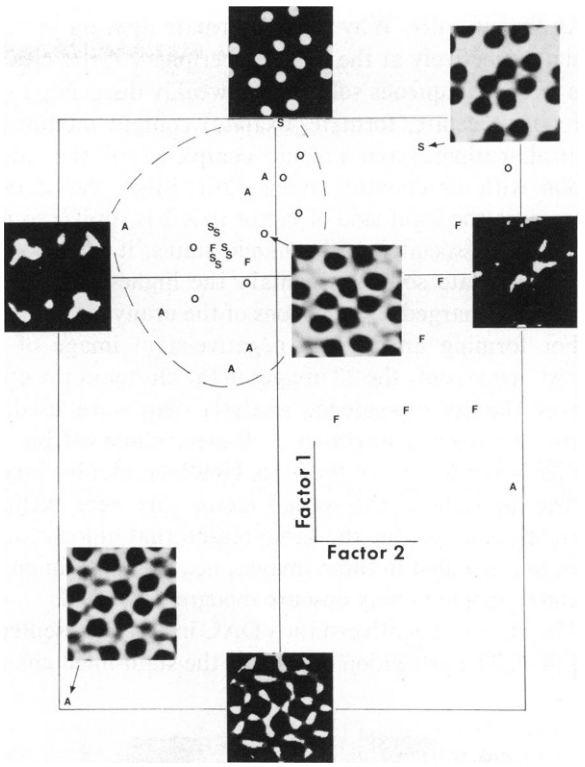

FIGURE 3 Map of uranyl-stained VDAC images in the plane defined by the first two factor axes of correspondence analysis. Importance images showing the variation in stain distribution are shown at either end of each factor axis. Images representing the upper-right, center, and lower-left of the map are also shown. The cluster of images used to form the average in Fig. 4 *A* is enclosed by a broken line. Labels: *A*, uranyl acetate; *F*, uranyl formate; *0*, uranyl oxalate; *S*, uranyl sulfate.

previously with anionic stains such as phosphotungstate (9). Trends in stain distribution associated with the next lower factor axes involve combinations of more localized differences, generally involving departures from p2-symmetry, and are not considered further here.

The staining pattern associated with the first factorial direction is not strongly dependent on the type of stain. Except for the outlier at the bottom of the first factor axis, the uranyl acetate images distribute fairly evenly along the top two-thirds of the axis. The other images also fall in the upper part of the map, with considerable overlap in the vertical positions of the differently stained images. It is possible that the staining trend represented by this factorial direction (stain inside vs. outside the channels) is a function (at least in part) of the thickness of the stain layer in which the arrays are embedded, i.e., the channel interiors of different VDAC arrays contain a constant 5-nm high cylinder of stain but may be covered by stain layers of different thicknesses.

The accumulation of stain in the immediate vicinity of the channels that is associated with factor axis 2 appears to be more strongly stain-dependent. Six of the eight uranyl formate images fall on the right 40% of factor axis 2, compared with only one each of the images of the other

three uranyl salts. Why uranyl formate appears to accumulate selectively at the channel periphery is not clear at this writing. Aqueous solutions of weakly dissociated uranyl salts (acetate, formate, oxalate) contain mixtures of neutral, cationic, and anionic complexes of the uranyl cation with its counter anions (26). Since the staining pattern on the right side of factor axis 2 is similar to that previously associated with anionic stains, it may be that uranyl formate solutions contain the highest fraction of negatively charged complex ions of the uranyl salts used.

For forming an average negative-stain image of the VDAC array, only the 22 images in the cluster at the upper left of the correspondence analysis map were used. In terms of factorial direction 1, these include all but the outlier at the bottom of the map. However, all nine images on the far right of the second factor axis were excluded from the average, for the same reason that anionic stains were not included in these images, i.e., excess stain on the channel periphery may obscure topographic detail.

The average negative-stain VDAC image is presented in Fig. 4 *A*. The projection of each of the stain-filled channel interiors appears roughly circular, with a diameter of ~2.5 nm. Each channel opening is bounded by a zone of stain exclusion that is radially nonuniform, i.e., the zones appear polygonal in shape and contain four or five discrete maxima. The loci of these maxima in the average image occur at positions in the channel cluster related by 180° rotation about the cluster center, even though p2 symmetry has not been imposed at any step in forming the average.

Low-Dose Imaging of Negatively Stained VDAC Arrays

The effect of radiation damage on projection images of negatively stained VDAC arrays was examined in imaging experiments in which the total accumulated dose was limited to 10^3 e/nm^2, vs. $>10^4$ e/nm^2 in normal image recording; see Materials and Methods section.

In general, there are detectable gains in Fourier resolution associated with decreased specimen irradiation of VDAC arrays negatively stained with 1% uranyl acetate. In optical or calculated diffraction patterns, the highest

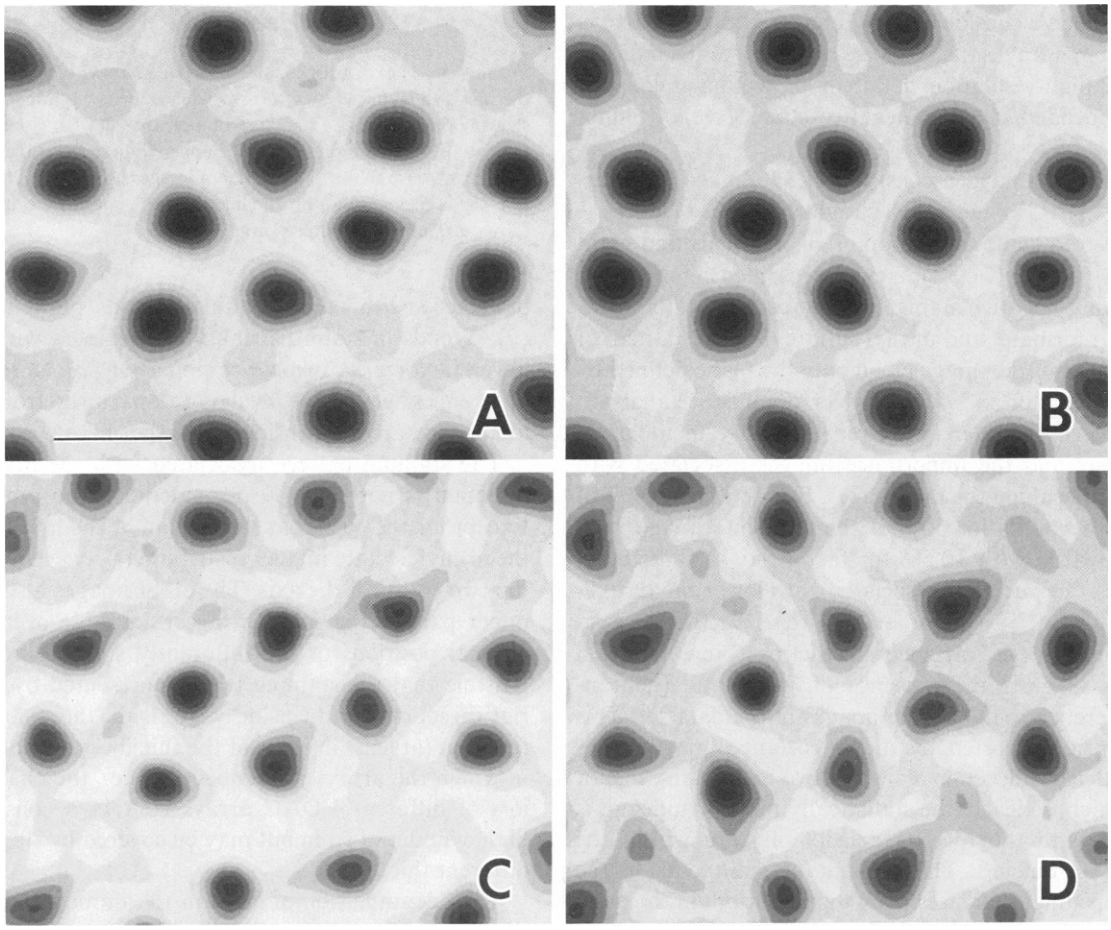

FIGURE 4 Projection images of VDAC arrays. (*A*) Average of 22 Fourier-filtered, high-dose images of uranyl-embedded arrays, based on correspondence analysis. (Total number of unit cells used to form average: ~10,000.) (*B–C*) Correlation averages of minimally irradiated VDAC arrays embedded in (*B*) 1% uranyl acetate (185 unit cells in average); (*C*) 0.1% uranyl acetate (170 unit cells in average); (*D*) 1% aurothioglucose (166 unit cells in average). The scale bar in (*A*) is 5 nm.

diffraction orders detected with low-dose images correspond to 1/(1.8 nm), compared with 1/(2.0 nm) in the best conventional-dose images. However, the somewhat higher Fourier resolution in these low-dose images does not result in new information about the VDAC array, as evidenced by the strong similarity between the best low-dose image of VDAC (Fig. 4 *B*) and the conventional-dose average image calculated in the preceding section (Fig. 4 *A*). Note that the resolution cutoffs of the individual Fourier-filtered images used to form the average of Fig. 4 *A* fell in the range 1/(2.5) nm to 1/(2.2) nm. In both average images, the projections of the channel interiors are similar in shape and size and are bounded by similarly shaped stain-excluding rims. The greatest difference between the two images is the lower accumulation of stain in the regions away from the channels in the low-dose image. Since this is a staining variation observed in conventional-dose images (i.e., along factor axis 1 in Fig. 3), it is probably not related to decreased specimen irradiation. In fact, other computer-averaged low-dose images of uranyl-embedded VDAC arrays (not shown) display darker stain accumulations in these regions.

Lattice Disorder: Correlation Averaging

As explained in the Methods section, cross-correlation of an image of a crystalline array with a reference image of one repeat unit of the array produces a map of the unit-cell positions in the field. Cross-correlation maps of high- or low-dose images of negatively stained VDAC arrays indicate that lattice disorder in the most coherent regions (such as those used for Fourier averaging) is on the order of ± 1 nm. Since this degree of disorder might limit attainable resolution in Fourier averages, correlation averaging (as described in Materials and Methods) has been used to form averages of low-dose electron images of negatively stained VDAC. In fact, the average low-dose uranyl image of Fig. 4 *B* was calculated by correlation averaging. As noted above, there is no significant difference between this image and the average obtained by Fourier filtration of high-dose images (Fig. 4 *A*).

Low Mass-Thickness Negative Stains

The above observations indicate that neither decreasing electron dose nor correcting for lattice disorder substantially changes the detail in electron images of negatively stained VDAC. To explore the effects of the nature of the stains on the projection images further, correlation averages were calculated from low-dose images of VDAC arrays that were air-dried in 0.1% uranyl acetate and in 1% aurothioglucose. The more dilute uranyl solution should result in less stain accumulation in the channel interior which, it is reasoned, might provide better detail about surface topography in the immediate vicinity of the channels. Advantages of embedding in gold-labelled glucose are possibly better structural preservation of biological specimens (27) and elimination of "positive staining" by ionic moieties in the stain solution.

Low-dose images of VDAC arrays negatively stained with either dilute uranyl acetate or aurothioglucose (Fig. 5 *A*) contain lower overall contrast than equivalent images of arrays embedded in conventional negative stains. Diffraction patterns from dilute-uranyl or aurothioglucose images (Fig. 5 *B*) do not extend past 1/(2.3 nm) in reciprocal space, i.e., not as good as the best low-dose images of conventionally stained VDAC arrays. Correlation averaging of fields of VDAC arrays in low mass-thickness stains (illustrated in Fig. 5) usually results in significantly improved resolution over Fourier filtration, although the Fourier cutoffs in power spectra of the final averages do not exceed those achieved in averages of arrays embedded in dense stain, i.e., ~1/(2.0 nm).

There are consistent differences between correlation averages of VDAC arrays in low mass-thickness stains and averages calculated from images of conventionally stained arrays. In particular, in correlation averages of VDAC arrays dried in both dilute uranyl (Fig. 4 *C*) and in aurothioglucose (Figs. 4 *D* and 5 *E*), the projections of the channel interiors are less round, more polygonal in shape and smaller (<2 nm in some directions) than those in 1%-uranyl images, and the channels are rimmed by white maxima that are relatively more intense than those that surround the channels in 1%-uranyl images. This greater contrast at subsidiary maxima is consistent with the expected decrease in opacity of the stain accumulations in the channel interiors. The white maxima in the 0.1%-uranyl images (Fig. 4 *C*) occur at or near the positions of the less intense maxima in the 1%-uranyl images (Figs. 4 *A* and *B*), consistent with their arising from common topological detail in the arrays. There is considerable agreement in the locations of maxima between the uranyl and aurothioglucose images, although much less than that among the uranyl images alone.

In general, Fourier and correlation averages of projection images of aurothioglucose-embedded VDAC arrays display at least as much variability as observed with uranyl stains, and have less apparent p2 symmetry. We will repeat these experiments using more sensitive recording emulsions (28) to determine whether these characteristics of aurothioglucose images are related to the greater beam sensitivity of this low-density negative stain (27).

Size of the VDAC Channel

As noted above, the size of the projected VDAC channel interiors decreases systematically from 3 nm for fully dissociated anionic stains (like phosphotungstate), to 2.5 nm for weakly dissociated uranyl salts, to 2 nm for dilute uranyl and aurothioglucose. The tendency of heavy-metal salts to penetrate proteins has been recognized as causing underestimation of protein size in negative stain imaging (e.g., reference 29). Conversely, the present results suggest that penetration of inorganic stains into the walls of a

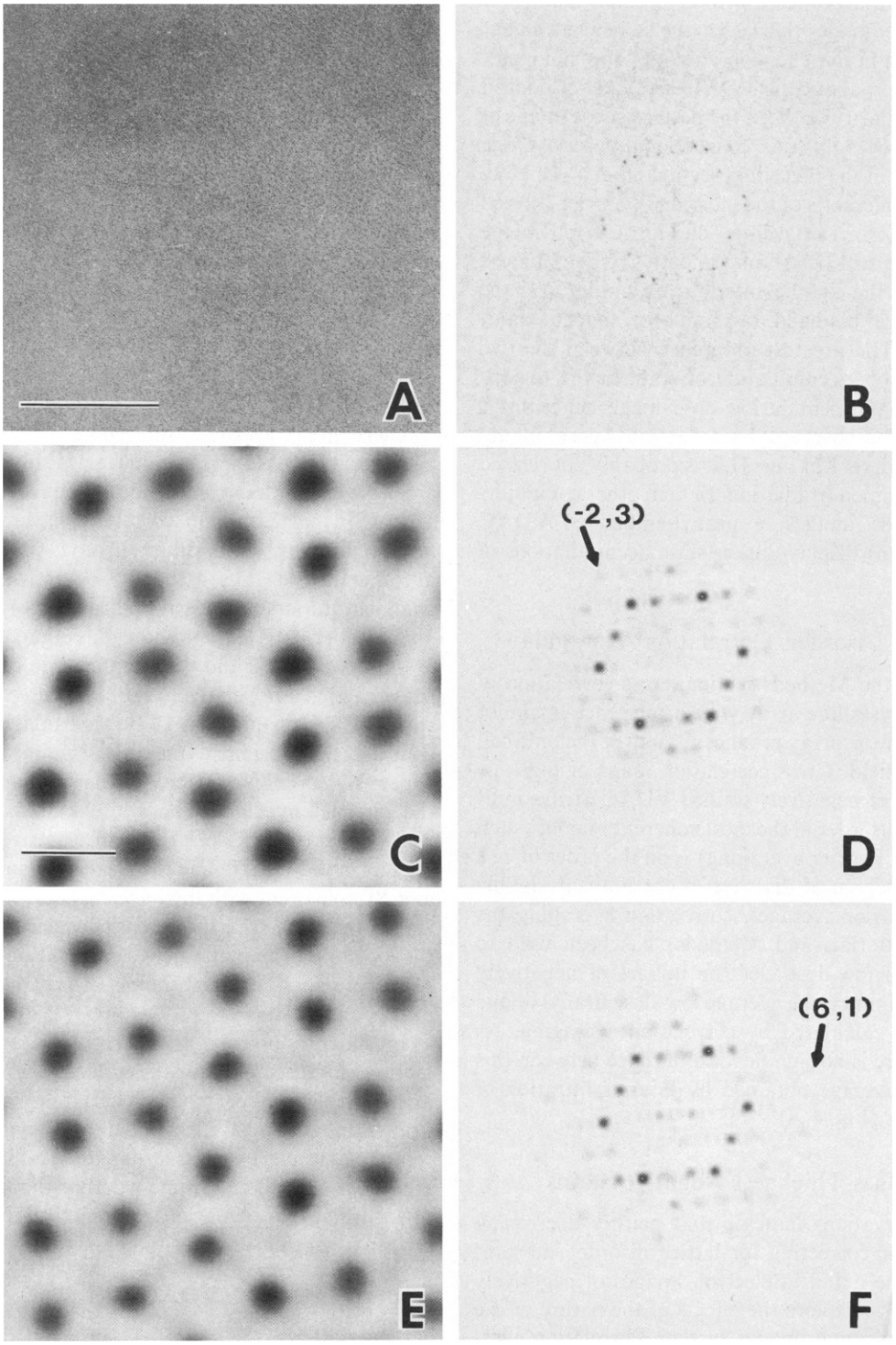

FIGURE 5 Computer-averaging of image of aurothioglucose-embedded VDAC array. (*A*) Original, low-contrast micrograph of field containing crystalline array. Scale bar = 0.1 μm. (*B*) Fourier power spectrum from 130 × 130 nm^2 region at upper-right of field in (*A*), showing two superimposed (but separable) parallelogram lattices, lattice angle = 99°. (*C*) Fourier filtration of image, using resolution limit imposed by cutoff of detectable maxima in power spectrum in (*B*), i.e., 1/(2.7 nm). (*D*) Power spectrum of (*C*); widest-angle reflection (arrow) corresponds to 1/(2.7 nm), as expected. (*E*) Correlation average over entire field of (*A*), using (*C*) as reference. Note improvement in Fourier resolution of corresponding power spectrum. The reflection indicated by arrow corresponds to 1/(2.1 nm). Number of unit cells included in averages: (*C*) 140, (*E*) 218. Scale bar in (*C*) is 5 nm.

channel may cause overestimation of the bore of the channel. The smaller stain accumulations in the VDAC arrays in the highest resolution averages obtained with nonionic aurothioglucose and dilute uranyl may well be a more faithful representation of the projected profile of the interior of the channels in crystalline VDAC. Interestingly, while the functional state of the VDAC channel in the crystalline state (i.e., "open" or "closed") is unknown, a channel bore of 2 nm is consistent with size of the "open" VDAC channel based on unit step-conductance (12).

Density Map of Unstained Crystalline VDAC

In first experiments, electron microscopic images have been recorded from thin aqueous layers of unstained mitochondrial outer membranes frozen directly in liquid nitrogen. Exposures were made with electron dose and objective lens defocus like those used in the minimal-dose, negative-stain experiments described above. In a few fields, membrane images were found which, despite patchy, noncrystalline appearances, have diffraction patterns with weak, low-order reflections characteristic of crystalline VDAC (Figs. 6 *A* and *B*). Despite the low signal-to-noise level in the images, correlation averaging techniques appear to be effective. Cross-correlation of these fields with suitable references (e.g., low-resolution Fourier averages of the fields or rotationally aligned negative-stain averages) indicate long-range order similar to that observed with negative-stain images. Correlation averages calculated over these fields contain detectable Fourier components of resolution $>1/(2\text{ nm})$ (Fig. 6 *D*). The image of Fig. 6 *C* represents a sum of correlation averages from three different image fields; p2 symmetry has been imposed on the final average.

Because the membranes in these projection images are unstained, contrast derives directly from the electron den-

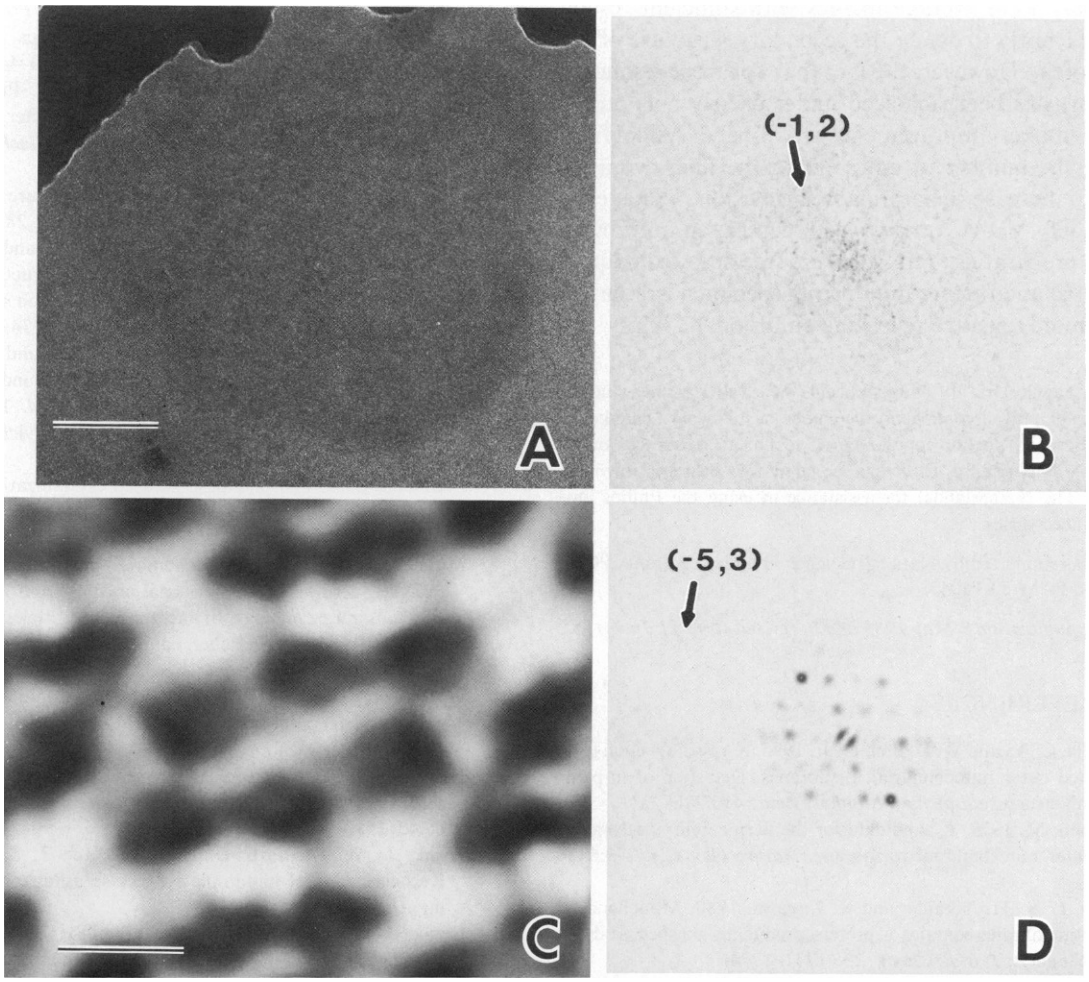

FIGURE 6 Computer averaging of images of ice-embedded VDAC array. (*A*) Original electron micrograph of membrane. Scale bar = 0.1 μm. (*B*) Fourier power spectrum from 130 × 130 nm^2 region at the upper-left quadrant of the membrane in (*A*). The reflection indicated by the arrow corresponds to 1/(4.7 nm). (*C*) Correlation average calculated over the membrane image in (*A*) plus another similar membrane image (number of unit cells in average: 400). This average image has been mirrored to correspond to those of Fig. 4 and p2-symmetry has been imposed. Scale bar = 5 nm. (*D*) Power spectrum corresponding to the correlation average of the membrane image in (*A*). Reflection indicated by the arrow corresponds to 1/(1.9 nm).

sities of the components of the VDAC array. The characteristic six-channel repeating unit of the parallelogram array is clearly visible as six closely packed, dark (i.e., protein) subunits which are bounded by patches of minimum density (i.e., lipid). The latter coincide exactly with regions in negative stain images previously assigned to phospholipid on the grounds that they stain lightly with uranyl (9) and shrink following prolonged phospholipase A_2 treatment (reference 18; see also Introduction). Finger-shaped regions of high density extend laterally across the low-density regions, appearing to connect adjoining groups of subunits. (These may represent long-range, interprotein contacts involved in stabilizing the channel arrays.) The projected density within each of the protein subunits is markedly uneven. Darkest maxima occur on the peripheries with regions of intermediate density near the centers, a distribution consistent with the projections of water-filled, protein channels.

There is no guarantee that the procedures applied above will someday yield average images with sufficient resolution ($>1/[1$ nm]) to define the secondary structure of the VDAC protein. However, the fact that apparent resolution of 1 (2 nm) has been achieved under clearly nonoptimal conditions makes improvement very likely. Aside from increasing the number of unit cells in the final averages, attempts to increase the attainable resolution in images of ice-embedded VDAC arrays will center on improving specimen preparation (e.g., faster freezing techniques, reference 16) and further minimizing specimen irradiation (by using more sensitive recording emulsions).

The authors thank Drs. T. Wagenknecht, M. Radermacher and A. Verschoor for helpful discussions in the course of this work. Thanks are due to Mr. Bernard Cognon for the expert technical assistance, and to Drs. W. M. A. Hax (Philips Electronics) and W. M. Busing (University of Limburg, The Netherlands) for assistance in using the Philips low-temperature accessories.

This study was supported by National Science Foundation grants PCM-83-15666 and PCM-83-13045.

Received for publication 3 May 1985 and in revised form 21 June 1985.

REFERENCES

1. Mannella, C. A., and W. D. Bonner, Jr. 1975. X-ray diffraction from oriented outer mitochondrial membranes. Detection of in-plane subunit structure. *Biochim. Biophys. Acta.* 413:226–233.
2. Colombini, M. 1979. A candidate for the permeability pathway of the outer mitochondrial membrane. *Nature (Lond.).* 279:643–645.
3. Zalman, L. S., H. Nikaido, and Y. Kagawa. 1980. Mitochondrial outer membrane contains a protein producing nonspecific diffusion channels. *J. Biol. Chem.* 255:1771–1774.
4. Schein, S. J., M. Colombini, and A. Finkelstein. 1976. Reconstitution in planar lipid bilayers of a voltage-dependent anion selective channel obtained from Paramecium mitochondria. *J. Memb. Biol.* 30:99–120.
5. Nikaido, H., M. Luckey, and E. Y. Rosenberg. 1980. Nonspecific and specific diffusion channels in the outer membrane of *Escherichia coli*. *J. Supramolec. Struct.* 13:305–313.
6. Mannella, C. A. 1982. Structure of the outer mitochondrial membrane: ordered arrays of porelike subunits in outer-membrane fractions from *Neurospora crassa* mitochondria. *J. Cell Biol.* 94:680–687.
7. Mannella, C. A., and M. Colombini. 1984. Evidence that the crystalline arrays in the outer membrane of *Neurospora crassa* mitochondria are composed of the voltage-dependent channel protein. *Biochim. Biophys. Acta.* 774:206–214.
8. Mannella, C. A., M. Colombini, and J. Frank. 1983. Structural and functional evidence for multiple channel complexes in the outer membrane of *Neurospora crassa* mitochondria. *Proc. Natl. Acad. Sci. USA.* 80:2243–2247.
9. Mannella, C. A., and J. Frank. 1984. Negative staining characteristics of arrays of mitochondrial pore protein: use of correspondence analysis to classify different staining patterns. *Ultramicroscopy.* 13:93–102.
10. Mannella, C. A., M. Radermacher, and J. Frank. 1984. Three-dimensional structure of mitochondrial outer-membrane channels from fungus and liver. *In* Proc. 42nd Annual Meeting Electron Microsc. Society America. G. W. Bailey, editor. San Francisco Press, San Francisco. 644–645.
11. Engel, A., D. L. Dorset, A. Massalski, and J. P. Rosenbusch. The low-resolution three-dimensional-structure of porin, a channel forming protein in *E. coli* outer membranes. *In* Proc. 41st Annual Meeting Electron Microsc. Society of America. G. W. Bailey, editor. San Francisco Press, San Francisco. 440–441.
12. Freitag, H., W. Neupert, and R. Benz. 1982. Purification and characterization of a pore protein of the outer mitochondrial membrane from *Neurospora crassa*. *Eur. J. Biochem.* 123:629–639.
13. Unwin, P. N. T., and G. Zampighi. 1980. Structure of the junction between communicating cells. *Nature (Lond.).* 283:545–549.
14. Makowski, L., D. L. D. Caspar, W. C. Philips, and D. A. Goodenough. 1984. Gap junction structures. V. Structural chemistry inferred from x-ray diffraction measurements on sucrose accessibility and trypsin susceptibility. *J. Mol. Biol.* 174:449–481.
15. Ross, M. J., M. W. Klymkowsky, D. A. Agard, and R. M. Stroud. 1977. Structural studies of a membrane-bound acetylcholine receptor from *Torpedo californica*. *J. Mol. Biol.* 116:635–659.
16. Unwin, N. 1985. Quaternary structure of the acetylcholine receptor. *Nature (Lond.).* 315:474–477.
17. Mannella, C. A. Phospholipase-induced crystallization of channels in mitochondrial outer membranes. *Science (Wash. DC).* 224:165–166.
18. Mannella, C. A. 1985. Mitochondrial outer-membrane channel (VDAC, porin)—two-dimensional crystals from *Neurospora*. *In* Methods in Enzymology. Biomembranes M. Biological Transport. S. Fleischer and R. Fleischer, editors. Academic Press, Inc., New York. In press.
19. Hallermayer, G., and W. Neupert. 1974. Lipid composition of mitochondrial outer and inner membranes of *Neurospora crassa*. *Hoppe-Seyler's. Z. Physiol. Chem.* 355:279–288.
20. Frank, J., B. Shimkin, and H. Dowse. 181. SPIDER—a modular software system for electron image processing. *Ultramicroscopy.* 6:343–358.
21. Frank, J., W. Goldfarb, D. Eisenberg, and T. S. Baker. 1982. Reconstruction of glutamine synthetase using computer averaging. *Ultramicroscopy.* 3:283–290.
22. Frank, J., A. Verschoor, and M. Boublik. 1982. Multivariate statistical analysis of ribosome electron micrographs. L and R lateral views of the 40S subunit from HeLa cells. *J. Mol. Biol.* 161:107–137.
23. Saxton, W. O. 1980. Matching and averaging over fragmented lattices. *In* Electron Microscopy at Molecular Dimensions. W. Baumeister and W. Vogell, editors. Springer-Verlag, Berlin, Heidelberg, and New York. 244–255.
24. Frank, J. 1982. New methods for averaging nonperiodic objects and

distorted crystals in biologic electron microscopy. *Optik*. 63:67–89.
25. Kessel, M., M. Radermacher, and J. Frank. 1985. The structure of the stalk surface layer of a brine pond microorganism: correlation averaging applied to a double layered lattice structure. *J. Microscopy*. In press.
26. Tzaphlidou, M., J. A. Chapman, and M. H. Al-Samman. 1982. A study of positive staining for electron microscopy using collagen as a model system. II. Staining by uranyl ions. *Micron*. 13:133–145.
27. Kuhlbrandt, W. 1982. Discrimination of protein and nucleic acids by electron microscopy using contrast variation. *Ultramicroscopy*. 7:221–232.
28. Munn, E. A. 1974. The application of the negative staining technique to the study of membranes. *In* Methods in Enzymology. S. Fleischer and L. Packer, editors. Academic Press, Inc., New York. 32:20–35.
29. Downing, K. H., and D. A. Grano. 1982. Analysis of photographic emulsions for electron microscopy of two-dimensional crystalline specimens. *Ultramicroscopy*. 7:381–404.

DISCUSSION

Session Chairman: Donald L. D. Caspar
Scribes: John Bramhall and William E. Royer, Jr.

AEBI: Can you tell us something about the subunit stiochiometry in the unit cell? We see the six pronounced channels which, as you indicated, are stain-filled holes in the negative stain. How many of the 30,000 d polypeptides do you have in the unit cell?

MANNELLA: From straightforward volume calculations, knowing the size of the polypeptide (30,000 d), and figuring the height of the membrane as 5–6 mn, there are between one and two polypeptides per channel. If you assume the channel diameter is 25 A, and 30% of the surface area is occupied by lipid, then it comes out as a monomer. But if the channel interior is smaller and there is less lipid, then it's a dimer. There are no relevant functional or crosslinking data yet available. However, the hydrodynamic data of Linden and Gelklerfors (1983. *Biophys, Biochim. Acta*. 736:125–129) indicate a dimer in the case of rat-liver channel.

AEBI: Do you have any information about how much the protein protrudes from the lipid bilayer? Do you have any shadowing or anything like that?

MANNELLA: We have not done shadowing on the channel arrays. We've done some freeze-eching on *Neurospora* mitochondria, and have seen no projections on outer membrane surfaces; however, these are low-resolution experiments. In negative-stain images of folded membranes there are no projections on either side. Without outer membranes from plant mitochondria, the lamellar spacings in x-ray diffraction patterns from oriented membranes are as low as 51 A. So it looks like this is a very flat membrane with no surface projections. In some ways this is an advantage.

AEBI: In your frozen hydrated projection images, do the dark areas represent protein ?

MANNELLA: The dark areas are the protein embedded in the membrane. There is no large superstructure of projecting material to obscure what is happening in the membrane. That's one of the reasons we feel this is an important model: it appears ideal for studying protein folding in a bilayer. With negative stain all you really see is the hole.

AEBI: What is the protein-to-lipid ratio?

MANNELLA: In the original membrane the mass ratio is 1:1, but phospholipase treatment removes at last 50% of the lipid, so the ordered membranes are more like 2:1. There are still many white (low-density) areas in the frozen hydrated image which presumably represent lipid.

AEBI: Your apparent channel sizes vary between 2 to 3 nm as judged from using different stains. How does this compare with the dimensions of the gap junction channel diameter?

MANNELLA: On average these appeart to be larger than the gap junction channels, which tend to have a goblet shape: they narrow down in the membrane interior. The mitochondrial outer membrane channels may be the largest channels for which a structure is available. Yet remember that they show anion selectivity.

AEBI: Qualitatively speaking, are your results similar to those obtained with the gap junction system by Baker et al. and Caspar et al.?

MANNELLA: One of the interesting aspects of their study was that they were able to show exclusion of certain anionic stains from the gap junction channels, so with these strains from the gap junction channels, only the superstructure of the channel was seen. This could be consistent with the cation selectivity of the channel.

CASPAR: Your channel seems to be relatively invariant under conditions of relatively extreme perturbation, whereas the gap junction is acutely sensitive to radiation damage and various perturbations introduced during specimen preparation. There are conditions where very little uranyl stain gets into the connexon channel, which suggests that the channel gate is normally closed in our specimins. If the gate is damaged, ions can get in and uranyl penetrates more than anionic stains.

STEWART: You suggest that one of the reasons you're not seeing the open channels is a matter of resolution. There is a problem with frozen hydrated samples which is that you are dealing wioth an image that is almost entirely phase contrast. Did you obtain the amplitudes that you used in your reconstruction from Fourier transforms of the object, or are your arrays sufficiently large and perfect to allow you to obtain amplitudes from electron diffraction?

MANNELLA: We have not yet attempted electron diffraction. The coherent patches that we see are limited in size (~ 200–300 unit cells), so the odds for getting useful diffraction patterns are pretty poor at this stage.

STEWART: Did you correct for the contrast transfer function?

STEWART: No. The reflections that were used in the Fourier average only went to ~ 30 A. We took these images under near focus conditions. We did not make any corrections to the low-frequency information.

STEWART: There is a surprising correspondence between the apparent holes seen with negative stain and the apparent protein seen with ice. I wonder to what extent positive staining might influence some of the results with phosphotungstate and uranyl acetate in that if you have an apparently featureless protein you may not get much modulation of the stain due to these negative stain effects. Have you tried washing the samples to see if there is a specific attachment of the stain?

MANNELLA: We did try this once during dark-field studies, and we found that the stain didn't wash off very readily, so the images were still dominated by what looked to be stain in the channels even after 2–3 washes. We should repeat these experiments using extensive, long-term washing.

DORSET: I was very interested in your observation of polymorphism. In matrix protein from *E. coli* we notice that there is a phase transition from the orthorhombic to small hexagonal, or vice versa. We see in Fourier-filtered images and electron-diffraction patterns a continuous diffuse scattering. Have you seen anything similar in your transforms?

MANNELLA: We haven't really looked for that, but we will now.

AEBI: How much significant (i.e., reproducible) structural detail can you get with your current samples and what are your prospects for improving your resolution?

MANNELLA: The fact that we were successful in applying correlation averaging to these relatively small arrays makes us think that we will be able to do pretty much the same things as can be done with much larger arrays. Currently we combine data from several arrays to maximize the signal-to-noise ratio and thus improve resolution. Of course we can also try to attain fusion of the small arrays, or use reconstitution of detergent-solubilized protein to form larger, multimicron-sized arrays.

AEBI: Do you have any indication that there is, in fact, higher-resolution structural detail preserved in the unit cells than what you are actually seeing?

MANNELLA: You are pointing out the difference between effective resolution in a sum like that of Fig. 6*c* and whether or not there are weak high-resolution Fourier components in the individual averages used to make this sum. The answer is yes. Fig. 6*d* shows that there are minor peaks in the power spectrum of an individual correlation average at 15–20 A even though the Fourier resolution of the final average (Fig. 6*c*) is between 15–30 A. We have not really optimized the dose in these experiments. By using more sensitive recording film and arrays that are larger and better-ordered, we should be able to decrease electron dose and so improve resolution in the individual averages. Although we do see indications of resolution better than 25 A in the power spectra of individual images, the Fourier components don't add constructively. Some image transforms have high resolution in one direction, others in a different direction. The net result is a lowered effective resolution. Basically we need many more unit cells to improve the final resolution.

CASPAR: Murray Stewart has made the point that the only way to see inside membranes with electrons is by using frozen hydrated samples; stains will give only surface information.

MANNELLA: In this context, it is instructive to compare the froxen hydrated image with the uranyl-stained image. Uranyl is known to bind weakly to phospholipid head groups. In the channel arrays, regions of bare lipid appear as lightly stained patches. Corresponding regions of bare lipid also appear as lightly stained patches. Corresponding regions of a frozen hydrated sample are seen as the lightest (lowest density) parts of the image. Comparing the ice image with the uranyl image makes it possible to detect what appear to be protein cross-bridges linking individual channels in the array. These connecting elements are quite long (5–6 nm). Because they appear as minima in the uranyl image, we conclude that they may be lying on the surface of the membrane. The question, of course, is what holds the channel complexes together in their lattice if in fact the complexes are entirely surrounded by lipid? These connecting bridges may well provide an answer. Clearly, the use of several different imaging technologies provided a good example of convergence of information on this system.